ACSNANO

www.acsnano.org

ARTICLE

Strain-Mediated Interfacial Dynamics during Au–PbS Core–Shell Nanostructure Formation

Kai-Yang Niu,[†] Miao Liu,[‡] Kristin A. Persson,[‡] Yu Han,[§] and Haimei Zheng*[,†,∥]

[†]Department of Materials Science and Engineering, University of California, Berkeley, California 94720, United States

[‡]Environmental Energy Technologies Division, Lawrence Berkeley National Laboratory, Berkeley, California 94720, United States

[§]Advanced Membranes and Porous Materials Center, Physical Sciences and Engineering Division, King Abdullah University of Science and Technology (KAUST), Thuwal 23955-6900, Kingdom of Saudi Arabia

[∥]Materials Sciences Division, Lawrence Berkeley National Laboratory, Berkeley, California 94720, United States

Supporting Information

ABSTRACT: **An understanding of the hierarchical nanostructure formation is of significant importance for the design of advanced functional materials. Here, we report the *in situ* study of lead sulfide (PbS) growth on gold (Au) nanorod seeds using liquid cell transmission electron microscopy (TEM). By tracking the formation dynamics of Au–PbS core–shell nanoparticles, we found the preferential heterogeneous nucleation of PbS on the ends of a Au nanorod prior to the development of a complete PdS shell. During PbS shell growth, drastic sulfidation of Au nanorod was observed, leading to large volume shrinkage (up to 50%) of the initial Au nanorod seed. We also captured intriguing wavy interfacial behavior, which can be explained by our DFT calculation results that the local strain gradient at the core–shell interface facilitates the mass transport and mediates reversible phase transitions of Au ↔ Au_2S during the PbS shell growth.**

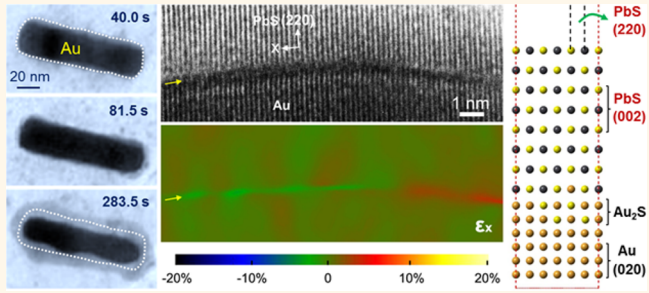

KEYWORDS: *liquid cell TEM, gold nanorod, core–shell nanostructure, heterogeneous growth, interfacial strain*

Metal–semiconductor core–shell nanostructures have attracted a lot of attention due to their potential applications in optoelectronic devices.[1] Typically, the metallic core improves charge separation and enhances absorption of light in the semiconductor during photo stimulation,[2] thus increasing the photocatalytic activity and the light harvesting efficiency of the semiconductor. When we tailor the differences in work function of the metal and semiconductor components and tunecore–shell nanostructures during synthesis, such as shell thickness and configuration of core and shell, improved synergetic performance may be realized. In addition, the interfacial structure may significantly influence the electronic properties of core–shell nanoparticles.[3]

Over the past decade, a wealth of noble metal–semiconductor core–shell nanostructures,[4] such as Ag–Cu_2O,[5] Ag–TiO_2,[6] Au–Cu_2O,[7,8] Au–TiO_2,[9] Au–SnO_2,[10] Au–PbS,[11] CoPt–CdSe,[12] *etc.*, have been synthesized for potential applications in optics, electronics, and catalysis. Nevertheless, some fundamental questions regarding the core–shell hybrid nanostructure formation remain to be addressed. For instance: How does the shell form initially, a uniform layer or an island? How does the core–shell interface evolve during shell growth? The answers to these questions may assist the future design and control of specific heterogeneous nanostructures.

Liquid cell transmission electron microscopy (TEM), allowing direct observation of rich dynamics of colloidal nanoparticle growth and self-assembly in liquids,[13−17] provides an opportunity to study the interfacial dynamics of core–shell nanostructures in real time. Here, we use gold–lead sulfide (Au–PbS) as a model system, where the synergetic effects of the gold surface plasmon resonance and the infrared absorption of lead sulfide provide the possibility to tune the Au–PbS core–shell nanostructures for various potential optoelectronic applications.[11] To develop a better understanding of the metal–semiconductor interfaces and the heterogeneous growth mechanisms, we investigated Au–PbS hybrid nanostructure formation in liquid (Figure S1). By tracking the growth trajectories of lead sulfide on a gold nanorod seed, we have observed unique growth dynamics, including the volume shrinkage of core particle and interfacial strain-driven mass transport and phase formation.

Received: April 6, 2016
Accepted: May 23, 2016
Published: May 23, 2016

DOI: 10.1021/acsnano.6b02331
ACS Nano 2016, 10, 6235–6240

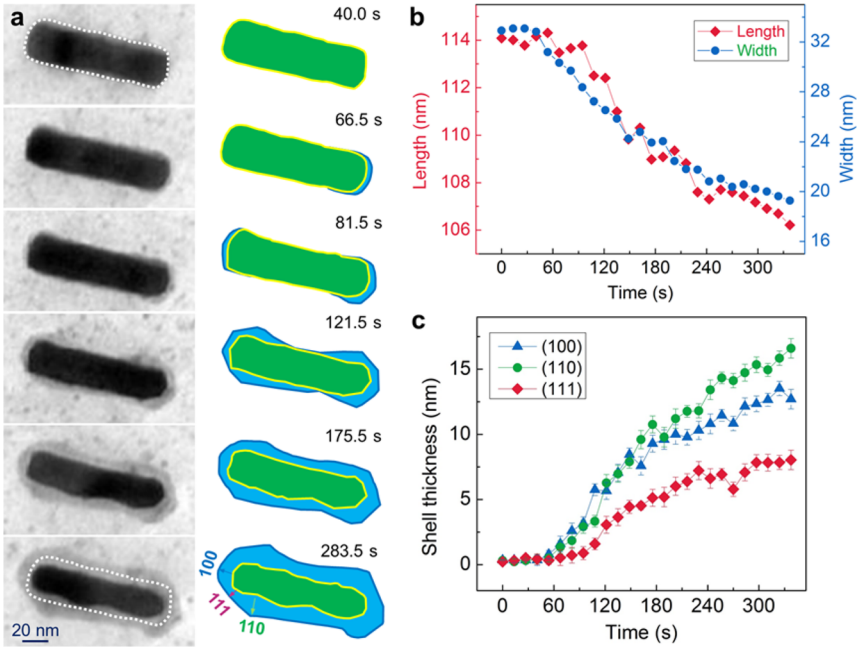

Figure 1. Heterogeneous nucleation and growth of lead sulfide on a gold nanorod. (a) TEM sequential images taken from Movie S1 and the corresponding schematic diagrams of the growth of a PbS shell on a gold nanorod. The white dashed lines on the TEM images define the contour of the original Au nanorod. (b) Length and width changes of gold nanorod during growth. (c) Dimension evolution of the shell thickness along three directions shown in (a).

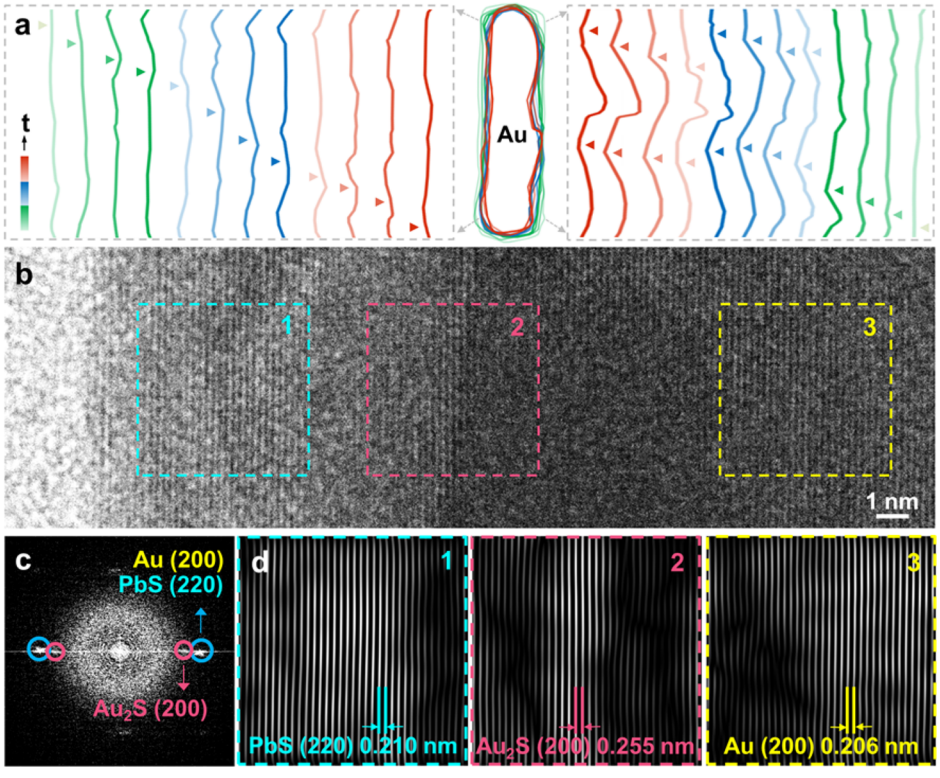

Figure 2. Interfacial structure and dynamic movement during core–shell nanoparticle formation. (a) Contours of the Au nanorod core, showing the evolution of core–shell interface (Movie S1). *t* stands for time. (b) HRTEM image of the Au–PbS core–shell interface. (c) FFT pattern from the dash frame areas in (b). (d) The corresponding inversed FFT images which indicate the three different phases in (b).

RESULTS AND DISCUSSION

The growth of PbS shell on a Au nanorod seed is captured in real-time, as shown in Figure 1a (also see Movie S1). At the early stages of reaction, Au nanorod slightly shrinks, indicating that the sulfidation reaction of Au nanocrystal has taken place on the surface (see detailed analysis of the interfaces in the later section). Subsequently, a thin layer of material with lighter contrast (*i.e.*, PbS; detailed analysis has been provided in a later section) appears at one end of the Au nanorod (see TEM

DOI: 10.1021/acsnano.6b02331
ACS Nano 2016, 10, 6235–6240

image at 66.5 s). At 81.5 s, both ends of the Au nanorod are covered by PbS. The continuous growth of PbS leads to a faceted dumbbell-shape, and the width and length of the Au nanorod are reduced about 15% and 5%, respectively (Figure 1b). Subsequently, the shell becomes more uniform while the Au nanorod continues shrinking. At 283.5 s, a smooth PbS shell with a thickness of 15−20 nm is achieved; the Au nanorod becomes much thinner with volume shrinkage of about 50% compared to the initial seed. We track the facet evolution of the PbS shell at one end of the nanorod, which shows relatively fast growth in the direction perpendicular to (110) and (100) facets resulting in the clear appearance of (111) facets (Figure 1c). It is noteworthy that a great number of homogeneously nucleated PbS nanoparticles serve as building blocks for the PbS shell construction *via* aggregative growth (Movie S2 and Figure S2).

During the Au−PbS core−shell nanostructure formation, dynamics of the core−shell interface evolution is also observed (Figure 1a). The marked triangles in Figure 2a highlight the pits at the interface displaying interfacial movement during the core−shell nanostructure growth and mass exchange across the interface. By tracking a series of Au nanorod contours as shown in Figure 2a, we find that the average rate of movement is about 0.19 nm/s. Figure 2b shows the high-resolution TEM image of the Au−PbS core−shell structure, where three different regions, *i.e.*, in the core, at the interface, and in the shell, are highlighted. Figure 2c displays the corresponding fast Fourier transform (FFT) pattern of the TEM image in Figure 2b, where the blue circles include both PbS and Au phases and the red circles demonstrate a possible stable phase of gold sulfide, *i.e.*, Au_2S.[18−20] Accordingly, three different phases, *i.e.*, Au, Au_2S, and PbS, displayed by the inversed FFT images, are identified in the core area, at the interface, and in the crystal shell, respectively.

In addition to the experimental observations, there is theoretical evidence suggesting that the formation of gold sulfide at the interfaces is favorable.[20,21] We perform first-principles calculations of the formation energy of three phases, *i.e.*, Au, Au_2S, and PbS (Supporting Text and Figure S4). On the basis of our calculation, PbS is the most stable phase among all investigated phases in the Pb−Au−S system with the lowest formation energy of −543 meV/atom. We found that the formation energy of Au_2S is 124 meV/atom lower than that of Au metal in the equilibrium/unstrained state, indicating that formation of Au_2S phase is thermodynamically preferred than formation of Au.[22]

Moreover, during the growth of shell on a core, strain can gradually build up around the interface.[23−26] It has been reported that the lattice strain can cause phase transformation in the Pt/Au core/shell nanocrystal,[26] and the interfacial strain gradient can facilitate the oxidation of Fe nanoparticles confined in an iron oxide shell.[23] We then examined the strain field at the core−shell interface by the Geometric Phase Analysis (GPA),[23,27−29] based on the high-resolution TEM images of the core−shell particles. The geometric phase obtained here is related to one-dimensional lattice displacement field $u_x(\mathbf{r})$ along the x direction, where $u_x(\mathbf{r}) = -(1/2\pi)P_g(\mathbf{r})\mathbf{g}$, and the $\mathbf{g}$ vector (220) of PbS was used for the displacement field determination. The corresponding strain field ($\boldsymbol{\varepsilon}_x$), given by the gradient of the displacement field along the x direction ($\boldsymbol{\varepsilon}_x = \delta u_x(\mathbf{r})/\delta_x$), indicating the local distortion of the lattice around the core−shell interface. As a result, an obvious strain gradient can be identified around the interfacial grain boundary (see Figure 3). We consider that the local strain generated from the PbS shell growth may have facilitated the mass transport and phase transitions at the interface, which results in the wavy interfacial dynamics as shown in Figure 2a.

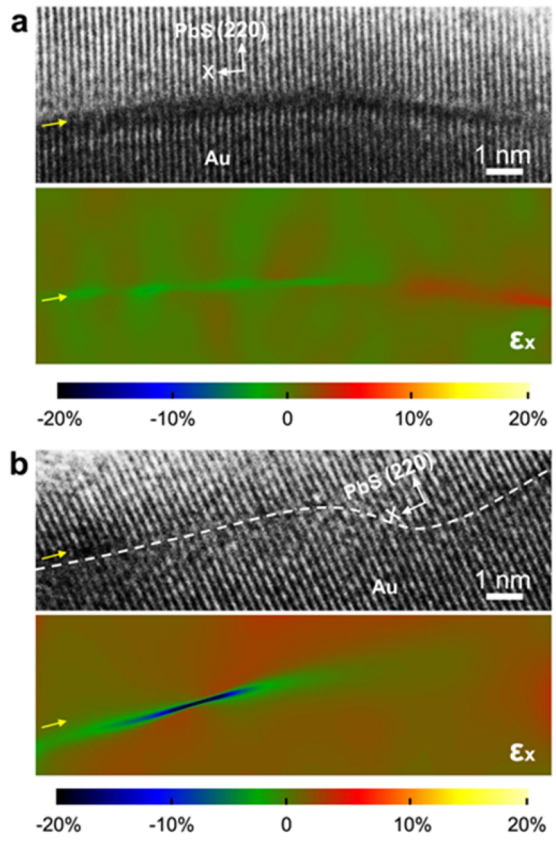

Figure 3. Strain map at the interfaces of Au−PbS core−shell particles. (a and b) High-resolution TEM images of the Au−PbS core−shell interfaces and the corresponding strain field ($\boldsymbol{\varepsilon}_x$) calculated from the (220) Bragg reflection of the PbS shell by geometric phase analysis (GPA). The yellow arrows mark at the interface to guide the eye; the white dash line in (b) indicates core−shell interface.

It is worth to mention that, for the epitaxial growth of PbS layers on the Au nanorods, two configurations with PbS (220) on Au (200) plane were observed, *i.e.*, parallel to the long axis of the Au nanorod (Figure 2, and Figure S3) and perpendicular to the long axis of the Au nanorod (Figure 3). Since the former growth configuration involves complex lattice mismatch in three-dimensional orientations adding complexity for the computation, we performed DFT calculations based on the second growth configuration (Figure 4a) to understand the role of local strain in the mass exchanges at core−shell interfaces.

We calculated the formation energy[30] *vs* biaxial strain for Au and Au_2S phases across the core−shell interface (Figure 4b and Supporting Text). Due to the higher stiffness of the PbS crystal, the softer core crystal lattice that is coherent with the stiffer PbS lattice can be strained (see more discussion in Supporting Text). Taking the strain energy into consideration, the relative thermodynamic stability between Au and Au_2S varies, and a tipping point of Au−Au_2S phase transition emerges, where the formation energy curves of Au and Au_2S cross over at ~4.20 Å, corresponding to 1.8% compressive strain with respect to the PbS equilibrium lattice parameter (4.26 Å) and 0.7% tensile strain with respect to Au equilibrium lattice parameter (4.17 Å). Since the formation energy variation between Au and Au_2S

DOI: 10.1021/acsnano.6b02331
ACS Nano 2016, 10, 6235−6240

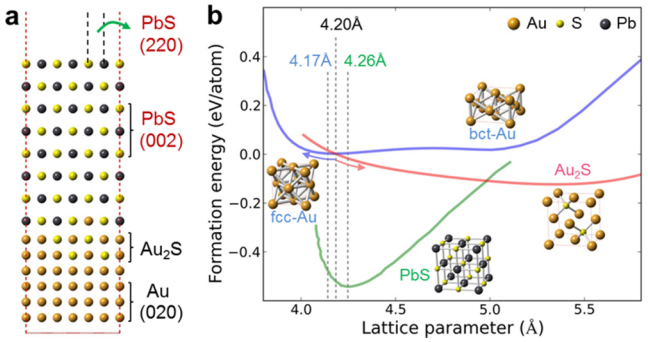

Figure 4. DFT calculation of the strain-driven phase transitions at the core−shell interface. (a) An atomistic model of the core−shell structure for the DFT calculation, which shows epitaxial growth of PbS (220) to Au (200) plane. (b) Formation energy of PbS, Au_2S, and Au under biaxial strain based on the structure model shown in (a). The atomistic crystal structures of each material are inserted to demonstrate the structures of three materials. The Au ↔ Au_2S phase transition point (4.20 Å) as well as the equilibrium lattice parameters of fcc-Au (4.17 Å) and PbS (4.26 Å) are marked in the figure with dashed lines.

phases around the tipping point is small (~25 meV/atom between 4.17 and 4.26 Å), the phase transition between Au and Au_2S is energetically easy, and subtle local strain variations may trigger the Au ↔ Au_2S phase transitions. As the PbS shell grows, the Au core lattice tends to be stretched, which facilitates the formation of Au_2S. Once the Au_2S phase forms, it is strained at the PbS equilibrium lattice parameter (4.26 Å). If the local compressive strain on Au_2S is increased (*i.e.*, lattice mismatch with PbS, defects[31] or electron beam effects[20]), the Au_2S could transform back to Au. Therefore, complex interfacial phenomena, such as large interfacial wavy motion in the growing core−shell nanostructure and selective sulfidation of Au nanorods, may occur during the core−shell nanostructure development where the strain gradient across the core−shell interface could facilitate the local phase transition and mass transport.[23]

On the basis of real-time observation and *ex situ* analysis, we propose a possible mechanism for the formation of Au−PbS core−shell nanostructures (Figure S5). Initially, upon electron beam irradiation, sulfur ions (S^{2-}) are released from the sulfur-containing source (TAA) into the solution (Figure S5a). These sulfur ions may react with the Pb^{2+} ions immediately, resulting in homogeneous nucleation of PbS nanoparticles in the solution (Movie S1). As to the heterogeneous nucleation, it is known that the as-synthesized Au nanorods are typically encapsulated by a bilayer of surfactant CTAB,[32,33] which makes the surface of Au nanorod positively charged.[32] Therefore, the negatively charged S^{2-} ions can approach the Au nanorods leading to sulfidation of the Au nanorods (Figures S5b and S6). In addition, it is found that the as-obtained Au nanorods are single crystalline with their side surfaces dominated by the {100} and {110} facets, and the nanorods ends terminated with the {111} facets.[34,35] It is expected that fewer CTAB ligands are absorbed on the {111} facets, which have weaker interaction with CTAB than the side facets of the nanorods.[36] In addition, the high curvature and relatively smaller facets on the Au nanorod ends might also promote the nucleation of gold sulfide on the nanorod ends. Consequently, the sulfidation of the Au nanorod takes place preferentially at the ends of a nanorod (Figure S5b). During the growth of PbS shell, the Au nanorod continues being sulfidized (Figure S5c), indicating further diffusion of S^{2-} ions into the Au nanocrystal, which is enhanced by the tensile strain exerted on the core.[23] As the Au_2S phase forms during PbS shell growth, the interdiffusion between Pb and Au ions occurs; thus, a PbxAuyS intermediate phase can be achieved at the interfaces (as indicated by the white outline in Figure S5c and the extra FFT diffraction spots in Figure S3a), which may reduce the strain thus the interfacial energy.

For the control experiment, we added extra surfactant of CTAB into the solution precursor. As shown in Figure 5, when

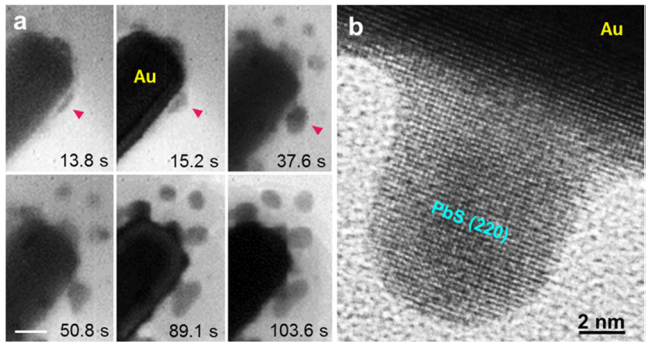

Figure 5. Effects of the CTAB surfactant on the heterogeneous growth of PbS on Au nanorods. (a) Heterogeneous nucleation and growth of PbS nanocrystals on a Au nanorod, when 150 μL of CTAB (0.5 M aqueous solution) is added. The red triangles indicate a PbS nanoparticle that grows into a rod shape, which is likely due to the surfactant effect. (b) HRTEM image of the as-grown single-crystal PbS nanocrystal on Au nanorod.

150 μL of CTAB (0.5 M aqueous solution) is added, heterogeneous nucleation and growth of single-crystal PbS nanocrystals on the Au nanorod are observed (Movie S3). It shows that PbS nuclei initially wet on the Au surface and it forms nanocrystals gradually. When 300 μL of CTAB (0.5 M aqueous solution) was used, PbS dendritic structure was achieved (Figure S7). The lack of a continuous PbS layer formation can be attributed to the high concentration of surfactants absorbed on the Au nanocyrstal surface.[36]

We conclude that the growth of Au−PbS core−shell heterostructures can be achieved by controlled solution chemistry during synthesis. The *in situ* observation allows the understanding of core−shell heterostructure formation, which enables feasible avenues for advanced materials design and engineering so that multifunctional hybrid nanostructures with modified properties can be obtained by tuning the structure of the core, shell, and core−shell interface.[37−39]

CONCLUSIONS

In summary, real-time imaging of the Au−PbS core−shell nanostructure growth was achieved using liquid cell TEM. Sulfidation of Au nanorods takes place prior to the PbS deposition, during which Au_2S phase is formed. The sulfidation reaction occurs preferentially at the ends of the nanorod and later it develops into a core−shell nanostructure. During the growth of PbS shell, the continuous sulfidation of Au nanorod leads to a large volume shrinkage up to 50% of the initial Au nanorod. Rich interfacial dynamics during the Au−PbS core−shell nanostructure formation has been observed. Driven by the interfacial strain gradient fluctuation, reversible phase transitions of Au ↔ Au_2S may happen across the core−shell interface, where a tensile strain facilitates the Au_2S formation

DOI: 10.1021/acsnano.6b02331
ACS Nano 2016, 10, 6235−6240

and a compressive strain may drive Au_2S back to Au metal. This study sheds light on the future control of advanced functional hybrid nanostructures.

METHODS

Liquid Cell TEM Sample Preparation. All chemicals and materials including lead(II) acetate ($Pb(CH_3COO)_2$), thioacetic acid (TAA), triethylene glycol (TEG), isopropyl alcohol (IPA), and cetyltrimethylammonium bromide (CTAB) were purchased from Sigma-Aldrich and used as received. Gold nanorods with diameter of ~40 nm and length of ~160 nm were purchased from Nanopartz, Inc. The deionized water was produced by Mili-Q integral water purification system. The primary precursor solution for the growth of lead sulfide was prepared by mixing 250 μL of $Pb(CH_3COO)_2$ aqueous solution (0.05 M), 250 μL of TAA aqueous solution (0.05 M), 150 μL of TEG, and 50 μL of IPA. The pH value of the solution was tuned below 3 by using acetic acid before loading into the liquid cell. To examine the effect of CTAB on the growth of the Au−PbS hybrid nanostructure, 150 and 300 μL of CTAB aqueous solution (0.5 M) were added into the primary solution for the *in situ* growth (Figure S1). The *in situ* growth and imaging of the Au−PbS hybrid nanostructures was carried out in homemade liquid cells, where the liquid precursors were sandwiched between two ultrathin silicon nitride membranes. The Au nanorods were loaded into the liquid cell first, followed by the loading of the precursor solution. The liquid cell was sealed for *in situ* TEM experiments.

***In Situ* and *ex Situ* TEM Imaging.** The *in situ* growth of lead sulfide was initiated by the electron beam in a JEOL 3010 TEM operated at 300 kV (thermionic electron source with a LaB_6 cathode). A Gatan Orius 833 CCD camera was used for high-throughput *in situ* imaging. The electron beam (with beam dose rate of 300 $e^{-}\cdot Å^{-2}\cdot s^{-1}$) passed through the silicon nitride window (1×50 μm^2), and induced the growth of lead sulfide on the gold nanorod seed. *In situ* movies were recorded at a rate of 30 frames/s by the open-sourced software VirtualDub embedded in the DigitalMicrograph software. *Ex situ* high-resolution TEM (HRTEM) images were acquired on 200 kV FEI F20 UT Tecnai TEM.

ASSOCIATED CONTENT

Supporting Information

The Supporting Information is available free of charge on the ACS Publications website at DOI: 10.1021/acsnano.6b02331.

TEM images of the as-grown Au−PbS hybrid particles, DFT calculation of the formation energy of Au, Au_2S and PbS phases (PDF)
Movie S1 (AVI)
Movie S2 (AVI)
Movie S3 (AVI)

AUTHOR INFORMATION

Corresponding Author

*E-mail: hmzheng@lbl.gov.

Notes

The authors declare no competing financial interest.

ACKNOWLEDGMENTS

We acknowledge the facility support of National Center for Electron Microscopy (NCEM) at the Molecular Foundry of Lawrence Berkeley National Laboratory, which is funded by the U.S. Department of Energy Basic Energy Sciences under the Contract No. DE-AC02-05CH11231. H.Z. thanks the support of DOE Office of Science Early Career Research Program. The computational work was supported by the Department of Energy's Basic Energy Sciences program - the Materials Project - under Grant No. EDCBEE. We also thank Dr. Karen Bustillo in NCEM for her help on the TEM analyzes.

REFERENCES

(1) Dutta, S. K.; Mehetor, S. K.; Pradhan, N. Metal Semiconductor Heterostructures for Photocatalytic Conversion of Light Energy. *J. Phys. Chem. Lett.* **2015**, *6*, 936−944.
(2) Jiang, R.; Li, B.; Fang, C.; Wang, J. Metal/Semiconductor Hybrid Nanostructures for Plasmon-Enhanced Applications. *Adv. Mater.* **2014**, *26*, 5274−309.
(3) Qin, W.; Hou, J.; Bonnell, D. A. Effect of Interface Atomic Structure on the Electronic Properties of Nano-Sized Metal−Oxide Interfaces. *Nano Lett.* **2015**, *15*, 211−217.
(4) Zhang, J.; Tang, Y.; Lee, K.; Ouyang, M. Nonepitaxial Growth of Hybrid Core-Shell Nanostructures with Large Lattice Mismatches. *Science* **2010**, *327*, 1634−8.
(5) Jing, H.; Large, N.; Zhang, Q.; Wang, H. Epitaxial Growth of Cu_2O on Ag Allows for Fine Control Over Particle Geometries and Optical Properties of Ag−Cu_2O Core−Shell Nanoparticles. *J. Phys. Chem. C* **2014**, *118*, 19948−19963.
(6) Hirakawa, T.; Kamat, P. V. Charge Separation and Catalytic Activity of Ag@TiO_2 Core-Shell Composite Clusters under UV-Irradiation. *J. Am. Chem. Soc.* **2005**, *127*, 3928−34.
(7) Kuo, C.-h.; Hua, T.-E.; Huang, M. H. Au Nanocrystal-Directed Growth of Au-Cu_2O Core-Shell Heterostructures with Precise Morphological Control. *J. Am. Chem. Soc.* **2009**, *131*, 17871−8.
(8) Zhang, L.; Blom, D. A.; Wang, H. Au−Cu_2O Core−Shell Nanoparticles: A Hybrid Metal-Semiconductor Heteronanostructure with Geometrically Tunable Optical Properties. *Chem. Mater.* **2011**, *23*, 4587−4598.
(9) Fang, C.; Jia, H.; Chang, S.; Ruan, Q.; Wang, P.; Chen, T.; Wang, J. (Gold Core)/(Titania Shell) Nanostructures for Plasmon-Enhanced Photon Harvesting and Generation of Reactive Oxygen Species. *Energy Environ. Sci.* **2014**, *7*, 3431−3438.
(10) Oldfield, G.; Ung, T.; Mulvaney, P. Au@SnO_2 Core-Shell Nanocapacitors. *Adv. Mater.* **2000**, *12*, 1519−1522.
(11) Lee, J.-S.; Shevchenko, E. V.; Talapin, D. V. Au−PbS Core−Shell Nanocrystals: Plasmonic Absorption Enhancement and Electrical Doping *via* Intra-Particle Charge Transfer. *J. Am. Chem. Soc.* **2008**, *130*, 9673−9675.
(12) Tian, Z. Q.; Zhang, Z. L.; Jiang, P.; Zhang, M. X.; Xie, H. Y.; Pang, D. W. Core/Shell Structured Noble Metal (Alloy)/Cadmium Selenide Nanocrystals. *Chem. Mater.* **2009**, *21*, 3039−3041.
(13) Zheng, H.; Smith, R. K.; Jun, Y.-w.; Kisielowski, C.; Dahmen, U.; Alivisatos, A. P. Observation of Single Colloidal Platinum Nanocrystal Growth Trajectories. *Science* **2009**, *324*, 1309−1312.
(14) Niu, K.; Liao, H.; Zheng, H. Revealing Dynamic Processes of Materials in Liquids Using Liquid Cell Transmission Electron Microscopy. *J. Visualized Exp.* **2012**, *70*, 50122.
(15) Liao, H.-G.; Zherebetskyy, D.; Xin, H.; Czarnik, C.; Ercius, P.; Elmlund, H.; Pan, M.; Wang, L.-W.; Zheng, H. Facet Development During Platinum Nanocube Growth. *Science* **2014**, *345*, 916−919.
(16) Sutter, E.; Jungjohann, K.; Bliznakov, S.; Courty, A.; Maisonhaute, E.; Tenney, S.; Sutter, P. *In Situ* liquid-Cell Electron Microscopy of Silver−Palladium Galvanic Replacement Reactions on Silver Nanoparticles. *Nat. Commun.* **2014**, *5*, 4946.
(17) Ross, F. M. Opportunities and Challenges in Liquid Cell Electron Microscopy. *Science* **2015**, *350*, aaa9886.
(18) Yoshizawa, K.; Iwahori, K.; Sugimoto, K.; Yamashita, I. Fabrication of Gold Sulfide Nanoparticles Using the Protein Cage of Apoferritin. *Chem. Lett.* **2006**, *35*, 1192−1193.
(19) Ishikawa, K.; Isonaga, T.; Wakita, S.; Suzuki, Y. Structure and Electrical Properties of Au_2S. *Solid State Ionics* **1995**, *79*, 60−66.
(20) Kundu, S.; Kundu, P.; Tendeloo, G. V.; Ravishankar, N. Au_2S_x/CdS Nanorods by Cation Exchange: Mechanistic Insights into the Competition between Cation-Exchange and Metal Ion Reduction. *Small* **2014**, *10*, 3895−3900.
(21) van Huis, M. A.; Figuerola, A.; Fang, C. M.; Béché, A.; Zandbergen, H. W.; Manna, L. Chemical Transformation of Au-

DOI: 10.1021/acsnano.6b02331
ACS Nano 2016, 10, 6235−6240

Tipped CdS Nanorods into AuS/Cd Core/Shell Particles by Electron Beam Irradiation. *Nano Lett.* **2011**, *11*, 4555−4561.
(22) Barton, M. D. The Ag-Au-S System. *Econ. Geol. Bull. Soc. Econ. Geol.* **1980**, *75*, 303−316.
(23) Pratt, A.; Lari, L.; Hovorka, O.; Shah, A.; Woffinden, C.; Tear, S. P.; Binns, C.; Kröger, R. Enhanced Oxidation of Nanoparticles through Strain-Mediated Ionic Transport. *Nat. Mater.* **2014**, *13*, 26−30.
(24) Cha, W.; Jeong, N. C.; Song, S.; Park, H.-j.; Thanh Pham, T. C.; Harder, R.; Lim, B.; Xiong, G.; Ahn, D.; McNulty, I.; Kim, J.; Yoon, K. B.; Robinson, I. K.; Kim, H. Core-Shell Strain Structure of Zeolite Microcrystals. *Nat. Mater.* **2013**, *12*, 729−34.
(25) Strasser, P.; Koh, S.; Anniyev, T.; Greeley, J.; More, K.; Yu, C.; Liu, Z.; Kaya, S.; Nordlund, D.; Ogasawara, H.; Toney, M. F.; Nilsson, A. Lattice-Strain Control of the Activity in Dealloyed Core-Shell Fuel Cell Catalysts. *Nat. Chem.* **2010**, *2*, 454−60.
(26) Kwon, S. G.; Krylova, G.; Phillips, P. J.; Klie, R. F.; Chattopadhyay, S.; Shibata, T.; Bunel, E. E.; Liu, Y.; Prakapenka, V. B.; Lee, B.; Shevchenko, E. V. Heterogeneous Nucleation and Shape Transformation of Multicomponent Metallic Nanostructures. *Nat. Mater.* **2015**, *14*, 215−223.
(27) Hÿtch, M.; Snoeck, E.; Kilaas, R. Quantitative Measurement of Displacement and Strain Fields from HREM Micrographs. *Ultramicroscopy* **1998**, *74*, 131−146.
(28) Hÿtch, M. J.; Putaux, J.-L.; Pénisson, J.-M. Measurement of the Displacement Field of Dislocations to 0.03 Å by Electron Microscopy. *Nature* **2003**, *423*, 270−273.
(29) Niu, K.; Frolov, T.; Xin, H. L.; Wang, J.; Asta, M.; Zheng, H. Bubble Nucleation and Migration in a Lead−Iron Hydr (oxide) Core−Shell Nanoparticle. *Proc. Natl. Acad. Sci. U. S. A.* **2015**, *112*, 12928−12932.
(30) Jain, A.; Ong, S. P.; Hautier, G.; Chen, W.; Richards, W. D.; Dacek, S.; Cholia, S.; Gunter, D.; Skinner, D.; Ceder, G.; Persson, K. a. Commentary: The Materials Project: A Materials Genome Approach to Accelerating Materials Innovation. *APL Mater.* **2013**, *1*, 011002.
(31) Kisielowski, C.; Krüger, J.; Ruvimov, S.; Suski, T.; Ager, J.; Jones, E.; Liliental-Weber, Z.; Rubin, M.; Weber, E.; Bremser, M.; Davis, R. Strain-Related Phenomena in GaN Thin Films. *Phys. Rev. B: Condens. Matter Mater. Phys.* **1996**, *54*, 17745−17753.
(32) Chen, Q.; Cho, H.; Manthiram, K.; Yoshida, M.; Ye, X.; Alivisatos, A. P. Interaction Potentials of Anisotropic Nanocrystals from the Trajectory Sampling of Particle Motion using *In Situ* Liquid Phase Transmission Electron Microscopy. *ACS Cent. Sci.* **2015**, *1*, 33−39.
(33) Ye, X.; Zheng, C.; Chen, J.; Gao, Y.; Murray, C. B. Using Binary Surfactant Mixtures to Simultaneously Improve Dimensional Tunability and Monodispersity in the Seeded-Growth of Gold Nanorods. *Nano Lett.* **2013**, *13*, 765−771.
(34) Orendorff, C. J.; Murphy, C. J. Quantitation of Metal Content in the Silver-Assisted Growth of Gold Nanorods. *J. Phys. Chem. B* **2006**, *110*, 3990−3994.
(35) Murphy, C. J.; Sau, T. K.; Gole, A. M.; Orendorff, C. J.; Gao, J.; Gou, L.; Hunyadi, S. E.; Li, T. Anisotropic Metal Nanoparticles: Synthesis, Assembly, and Optical Applications. *J. Phys. Chem. B* **2005**, *109*, 13857−13870.
(36) Gao, J.; Bender, C. M.; Murphy, C. J. Dependence of the Gold Nanorod Aspect Ratio on the Nature of the Directing Surfactant in Aqueous Solution. *Langmuir* **2003**, *19*, 9065−9070.
(37) Chen, J.; Zhang, R.; Han, L.; Tu, B.; Zhao, D. One-Pot Synthesis of Thermally Stable Gold@Mesoporous Silica Core-Shell Nanospheres with Catalytic Activity. *Nano Res.* **2013**, *6*, 871−879.
(38) Wang, J.; Huang, H.; Zhang, D.; Chen, M.; Zhang, Y.; Yu, X.; Zhou, L.; Wang, Q. Synthesis of Gold/Rare-Earth-Vanadate Core/Shell Nanorods for Integrating Plasmon Resonance and Fluorescence. *Nano Res.* **2015**, *8*, 2548−2561.
(39) Zhao, Y.; Zhang, Y.; Zhao, H.; Li, X.; Li, Y.; Wen, L.; Yan, Z.; Huo, Z. Epitaxial Growth of Hyperbranched Cu/Cu_2O/CuO Core-Shell Nanowire Heterostructures for Lithium-Ion Batteries. *Nano Res.* **2015**, *8*, 2763−2776.

DOI: 10.1021/acsnano.6b02331
ACS Nano 2016, 10, 6235−6240